energies

MDPI

Article

Contribution of Voltage Support Function to Virtual Inertia Control Performance of Inverter-Based Resource in Frequency Stability

Dai Orihara [1,*], Hiroshi Kikusato [1], Jun Hashimoto [1], Kenji Otani [1], Takahiro Takamatsu [1], Takashi Oozeki [1], Hisao Taoka [1], Takahiro Matsuura [2], Satoshi Miyazaki [2], Hiromu Hamada [2] and Kenjiro Mori [2]

[1] Renewable Energy Research Center, National Institute of Advanced Industrial Science and Technology, 2-2-9, Machiikedai, Fukushima 963-0298, Japan; hiroshi-kikusato@aist.go.jp (H.K.); j.hashimoto@aist.go.jp (J.H.); k.otani@aist.go.jp (K.O.); takamatsu.1849@aist.go.jp (T.T.); takashi.oozeki@aist.go.jp (T.O.); hisao.taoka@aist.go.jp (H.T.)

[2] TEPCO Research Institute, Tokyo Electric Power Company Holdings, 4-1, Egasaki-cho, Tsurumi-ku, Yokohama 230-0002, Japan; matsuura.takahiro@tepco.co.jp (T.M.); miyazaki.satoshi@tepco.co.jp (S.M.); hamada.hiromu@tepco.co.jp (H.H.); mori.kenjiro@tepco.co.jp (K.M.)

* Correspondence: oriahra.dai@aist.go.jp

Abstract: Inertia reduction due to inverter-based resource (IBR) penetration deteriorates power system stability, which can be addressed using virtual inertia (VI) control. There are two types of implementation methods for VI control: grid-following (GFL) and grid-forming (GFM). There is an apparent difference among them for the voltage regulation capability, because the GFM controls IBR to act as a voltage source and GFL controls it to act as a current source. The difference affects the performance of the VI control function, because stable voltage conditions help the inertial response to contribute to system stability. However, GFL can provide the voltage control function with reactive power controllability, and it can be activated simultaneously with the VI control function. This study analyzes the performance of GFL-type VI control with a voltage control function for frequency stability improvement. The results show that the voltage control function decreases the voltage variation caused by the fault, improving the responsivity of the VI function. In addition, it is found that the voltage control is effective in suppressing the power swing among synchronous generators. The clarification of the contribution of the voltage control function to the performance of the VI control is novelty of this paper.

Keywords: frequency stability; inverter-based resource; virtual inertia; grid-forming; grid-following; PLL; RoCoF

Citation: Orihara, D.; Kikusato, H.; Hashimoto, J.; Otani, K.; Takamatsu, T.; Oozeki, T.; Taoka, H.; Matsuura, T.; Miyazaki, S.; Hamada, H.; et al. Contribution of Voltage Support Function to Virtual Inertia Control Performance of Inverter-Based Resource in Frequency Stability. *Energies* **2021**, *14*, 4220. https://doi.org/10.3390/en14144220

Academic Editor: Woojin Choi

Received: 8 June 2021
Accepted: 8 July 2021
Published: 13 July 2021

1. Introduction

The increasing penetration of renewable energy resources causes instability in power systems due to the uncertainty of them. In particular, the total amount of inertia decreases when inverter-based resources (IBRs) displace large amounts of energy generation from synchronous generators. In this situation, the phase-angle stability and frequency stability worsen, and reserve power needs to increase to compensate for the inertia reduction and to maintain a stable power supply in the future. In addition, the voltage stability is also affected, because conventional IBRs are not controlled to maintain a voltage, unlike synchronous generators comprising automatic voltage regulators (AVRs). In some systems, a voltage support function, which has been recognized as a crucial part in developing an IBR-dominated system, is required for an IBR that is newly connected to the grid [1,2]. Additionally, the influence on the protection system needs to be discussed. the IBR cannot provide a large shunt current for a system fault compared with a synchronous machine, which might cause incorrect fault detection.

The virtual inertia (VI) control, which makes the IBR act as a synchronous generator, can be used to address the aforementioned drawback of an IBR. The IBR with VI control changes its output according to the dynamics of the synchronous generator and contributes to the power system stability due to its ability to provide an inertial response, frequency response, and voltage control function similar to a synchronous generator. There are numerous types of implementation methods for VI control [3–5], which are divided into two types: grid-following (GFL) and grid-forming (GFM). GFL and GFM are categories of control of the voltage source converter (VSC) and do not directly mean VI control. The GFL and GFM types control the IBR to act as the current and voltage sources, respectively. A detailed common definition of GFL and GFM has not been established and is still under discussion [6–13]. Moreover, both the GFL-type VI control (VI-GFL) and GFM-type VI control (VI-GFM) are effective in compensating for the inertia reduction, but VI-GFL cannot perform well under low inertia conditions. The phase-locked loop (PLL), which is used in the GFL-type controller for detecting phase angle and frequency at the point of interconnection (POI), cannot maintain stable operations because of the rapid variation of the phase angle and frequency caused by a disturbance in such conditions [14–16]. Thus, VI-GFL alone cannot maintain stability and requires a certain amount of VI-GFM at a high IBR penetration level.

Several studies on VI control have discussed frequency stability owing to the effect of inertia reduction on it. The blackout in Australia in 2016 [17] and the power cut in the UK in 2018 [18] emphasize the importance of countermeasure for frequency stability. These studies were primarily focused on clarifying the contribution of the VI control to the reduction of frequency variation. Previous studies [9,19–22] compared various VI control implementations using a time-domain simulation method. In addition, the implementation adapted to the characteristics of renewable energy sources [23,24], control parameter optimization [25], and the estimation of effective inertia [26] have been investigated to enhance the VI control performance and applicability. Other studies have addressed the influence on rotor-angle stability [27–30] and small-signal stability [22,31,32].

This study aims to analyze the performance of VI control in reducing the frequency variation and to clarify the contribution of the voltage control function of the GFL-type inverter to the performance of the VI-GFL. The voltage control function changes the reactive power output of the IBR and can be activated simultaneously with the VI-GFL, which controls the active power output. The activation of the voltage control function is expected to improve the performance of the VI-GFL, because stable voltage conditions enhance the active power controllability. However, its effectiveness has not been addressed in other studies. In this study, the contribution of VI control to the frequency and voltage stability is analyzed by focusing on the VI-GFL with and without the voltage control function and the VI-GFM under several conditions with different IBR penetration levels through electromagnetic transient simulations. The novelty of the paper is to clarify the performance improvement of the VI-GFL offered by the voltage control function.

The remainder of the paper is organized as follows: Section 2 describes the power system model for the simulation study. The IBR controller model is explained in Section 3. Section 4 presents the simulation conditions and control parameters of the IBR. Section 5 presents the simulation results and the VI control performance evaluation. Finally, Section 6 concludes the paper.

2. Power System Model

In this study, the contribution of the VI control was evaluated through three types of simulations: Step 1, Step 2, and Step 3. The Step 1 simulation is a base case simulation using synchronous generators and not IBRs. On the other hand, the Step 2 simulation replaces a part of the synchronous generators with IBRs, which do not have VI control, to analyze the power system stability without any countermeasures for inertia reduction. Finally, the Step 3 simulation implements IBRs with VI control to analyze the effectiveness

of the VI control by analyzing three types of algorithms: VI-GFL with/without the voltage control function and VI-GFM.

2.1. Network Model

The power system model for the simulation study, which is based on the IEEE 9-bus system model [33], is described in this section, as shown in Figure 1. As previously stated, the performance of the VI control was evaluated through Steps 1–3 simulations using different power system models in each step. The model for the Step 1 simulation was composed of synchronous generators, and all the power sources—namely, S1, S2, S3, and SD—were synchronous generators, indicating that this model was a conventional synchronous generator-dominated system. Meanwhile, in the Step 2 simulation, the power source S3 was a normal inverter that did not have any controller that contributed to the frequency regulation instead of a synchronous generator. Finally, the IBR with the VI control was connected to S3 in Step 3. The three types of VI control methods analyzed in this step are explained in Section 3. Moreover, the power source SD was a small-scale synchronous generator that was tripped at a certain time in the simulation as a disturbance. Lastly, the load was modeled as a constant current for the active load and a constant impedance for the reactive load. The impedances of the transmission lines and transformers are shown in Figure 1.

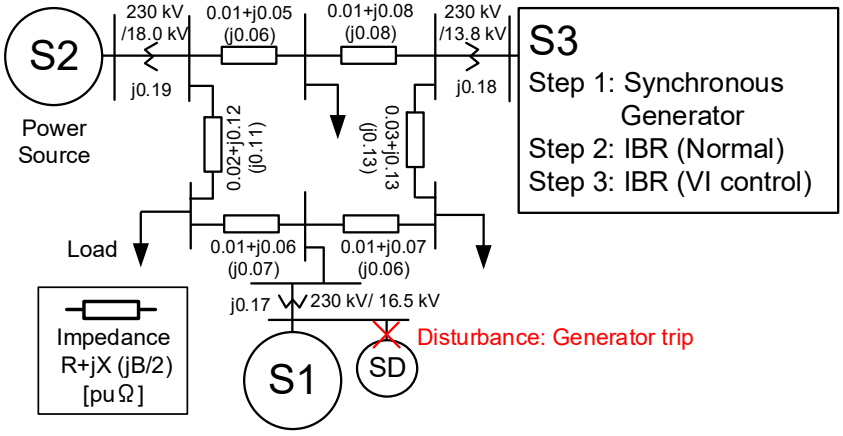

Figure 1. Power system model.

In this model, the IBR model represented an aggregated one and connected to a high-voltage bus, while the IBRs were widely distributed, and most of them were actually connected to the low-voltage class. The purpose of the simulation study was to show how the IBRs should perform as a mass for power system stabilization.

2.2. Synchronous Generator Model

The simulation of the synchronous generator model with two damping windings on the q-axis equivalent circuit [33] was performed using PSCAD/EMDC, which is an electromagnetic transient analysis tool. Both the speed governor and excitation controller were modeled as controllers for the synchronous generator. In addition, this simulation study did not include both the secondary control and those with longer control cycles, because this study focused on the transient system behavior within 10 s after the occurrence of the disturbance. Figure 2 shows a model of the speed governor and turbine [34]. The time delay due to the governor, control valve, and turbines was considered in the model. P_{ref} was the load reference that was managed by the central control system of the transmission system operator (TSO). Meanwhile, Figure 3 shows the excitation controller model [34]. The excitation voltage was controlled to maintain the terminal voltage at the reference. In addition, the power system stabilizer (PSS) model was included in the excitation system to dampen the short-period oscillations.

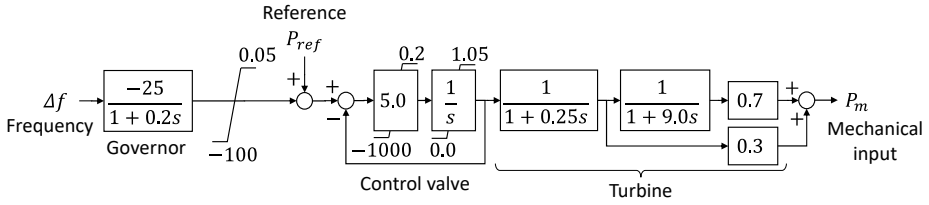

Figure 2. Speed governor and turbine model.

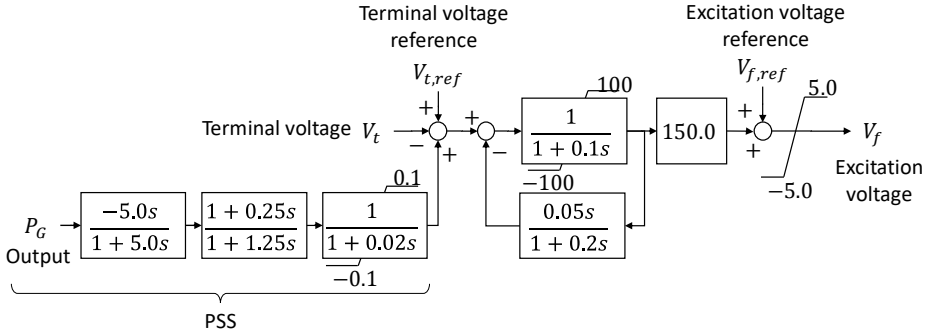

Figure 3. AVR model comprising PSS.

2.3. IBR Model

The IBR was modeled as a three-phase voltage source whose magnitude and phase angle followed the reference from the IBR controller, as shown in Figure 4. This is called the average model [35], which is conventionally used in analyzing several phenomena involving the fundamental wave component at high accuracy but not including the second and subsequent harmonics. This indicated that harmonics were not addressed in the simulation. Moreover, the DC power source and capacitance were not modeled based on the assumption that the DC power source can maintain a constant DC voltage and change its output required by the IBR controller without any time delay and at a high accuracy. This assumption was made because this study focused on the influence of inverter control on the AC power system stability. The IBR model was connected to the power grid model as power source S3 in the Steps 2 and 3 simulations.

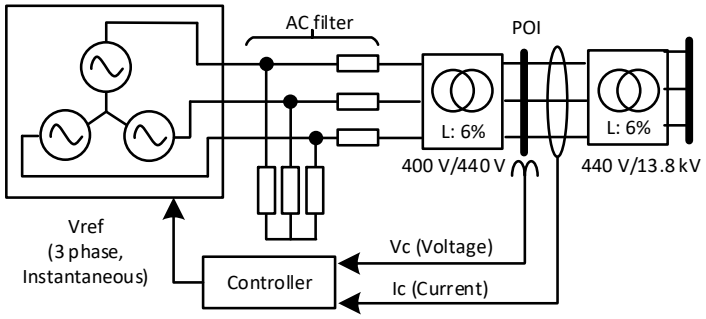

Figure 4. Average IBR model.

3. IBR Controller Model

This section presents the inverter controller model. Specifically, Section 3.1 presents the conventional inverter controller model used in the Step 2 simulation, Section 3.2 shows the VI-GFL model, and Section 3.3 presents the VI-GFM model.

3.1. Conventional IBR Controller

Inverters for the interconnection of IBRs, such as photovoltaic generations (PVs), wind generations, and battery energy storage systems (BESSs), are controlled to maintain the

output power at the control reference given by its upper controller. For example, PVs and wind generations are equipped with maximum power point tracking (MPPT), and BESS has an energy management system (EMS) to monitor and control the energy storage system. Figure 5 shows the controller model of the conventional inverter. In this model, the voltage and current are dealt with in the form of d- and q-axes components. Specifically, Figure 5a shows Park's transformation of the input or output signals of the controller. The voltage at the POI V_c and the output current I_C are input signals and decomposed into d- or q-axis components. The voltage reference V_{ref} is the controller output and is composed of these components through inverse Park's transformation. The reference phase angle for Park's transformation is measured from V_C by PLL, as shown in Figure 5b [36]. Meanwhile, Figure 5c shows the main controller as a series connection of the power and current controllers. The active and reactive power control blocks manage the d- and q-axes currents through the PI controller, respectively, and the decoupled current control block manages the voltage reference to ensure that the IBR outputs the desired current [37]. The current limitation is defined by Equations (1) and (2) to limit the magnitude of the current reference and not exceed the current capacity.

$$I_{d,lmt} = I_{lmt} \tag{1}$$

$$I_{q,lmt} = \sqrt{I_{lmt}^2 - I_{d,lmt}^2} \tag{2}$$

where $I_{d,lmt}$ and $I_{q,lmt}$ are the maximum magnitudes of the d-and q-axes currents, respectively. The d-axis current reference $I_{c,d,ref}$ is constrained by the maximum available current I_{lmt}, while the q-axis current reference $I_{c,q,ref}$ is constrained by the remaining capacity to prioritize the active power control. The conventional control changes the output voltage for the system voltage change to maintain the output power by ensuring that the angle difference does not change. That is, the output voltage "follows" the system voltage, and this is because the conventional control is categorized as the GFL-type.

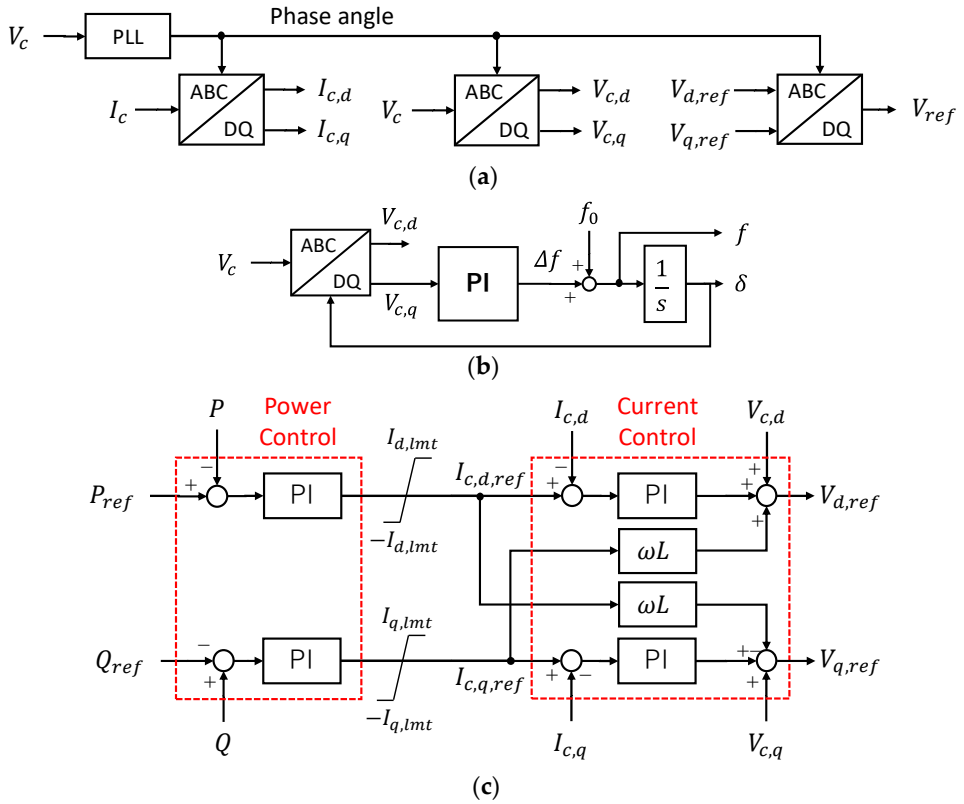

Figure 5. Controller model of the conventional converter. (**a**) Park's transformation of the signals addressed in the controller, (**b**) the PLL model, and (**c**) a block diagram.

3.2. Grid-Following-Type Virtual Inertial Control (VI-GFL)

In this study, the VI-GFL model consisted of the VI function and speed governor, which is the primary frequency controller. Figure 6 shows the controller model of the VI-GFL, which manages the active power output to be similar to that of the synchronous generator. The algorithm is based on the dynamics of the synchronous generator shown below [33].

$$M\frac{df(t)}{dt} = P_m(t) - P_e(t) \tag{3}$$

where M is the inertia constant, f is the rotating frequency of the generator, P_m is the machinery input power, and P_e is the electrical output. $M(df(t)/dt)$ represents the inertial response of the synchronous generator. The VI function is performed by the active power change corresponding to the inertial response. The differentiation of the frequency is computed in the controller from the measured frequency as the slope between the present value and the value just before the time window T_W. Moreover, a low-pass filter with a time constant T_f is included to remove noise on the frequency detected by the PLL. The reference of the VI function ΔP_{VI} is computed by multiplying the virtual inertia constant M_{VI} by the frequency differentiation. The speed governor function is modeled as a proportional controller of the frequency, as in the synchronous generator. The reference ΔP_{GV} was computed using Equation (4).

$$\Delta P_{GV} = -K_{GV}\{f(t) - f_0\}, \tag{4}$$

where K_{GV} is the governor gain and f_0 is the base frequency. The original active power reference P_{ref} is modified to P'_{ref} by ΔP_{VI} and ΔP_{GV}. The speed governor of the synchronous machine has a deadband and responds after the frequency surpasses it, but the governor function of the VI-GFL does not have it and is expected to respond to a disturbance very quickly.

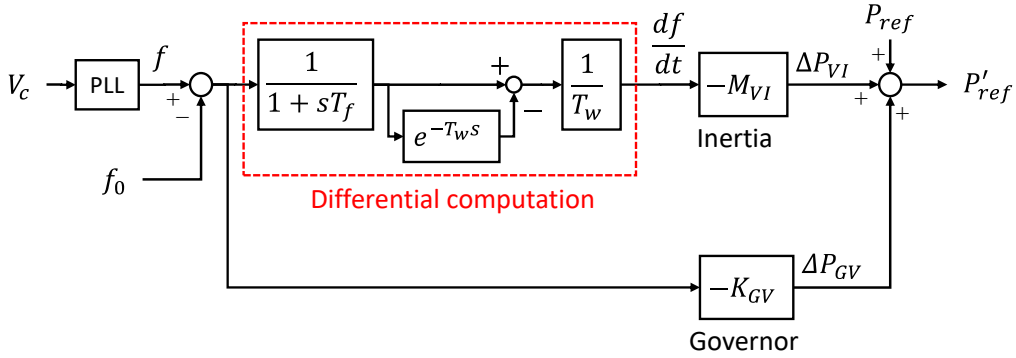

Figure 6. Controller model of the VI-GFL.

This study focuses on the contribution of the reactive power control in regulating the voltage to the performance of the VI function. Figure 7 shows the droop voltage controller, which modifies the reactive power command Q_{ref} based on the control deviation of the POI voltage with the proportional gain $K_{V,GFL}$.

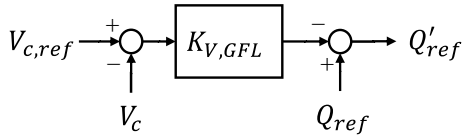

Figure 7. Reactive power controller optionally embedded in the GFL-type controller for voltage regulation.

3.3. Grid-Forming Virtual Inertia Control (VI-GFM)

Figure 8 shows the VI-GFM controller model, which is defined by Equation (3) using a different methodology than the VI-GFL. The frequency deviation Δf is computed from the measured active power P, while the VI-GFL controller computes the active power command P'_{ref} from the measured frequency at the VI and governor function block. The governor function of the VI-GFM was also modeled without the deadband, the same as that of the VI-GFL. The frequency command is transformed by integrating into the command of the phase angle of the internal induced voltage δ_{ref}. The magnitude of the induced voltage E_{ref} is managed by the AVR block, thereby maintaining the POI voltage at the reference $V_{c,ref}$ modified by the droop controller. The internal induced voltage $\boldsymbol{E_{ref}}\left(= E_{ref}\angle\delta_{ref}\right)$ is transformed to the output current order through a virtual impedance block according to Equation (5), indicating that the controller assumes that the voltage source is connected to the POI through the impedance $r_{vir} + jx_{vir}$.

$$\boldsymbol{I_{c,ref}} = \frac{\boldsymbol{E_{ref}} - \boldsymbol{V_c}}{r_{vir} + jx_{vir}} \tag{5}$$

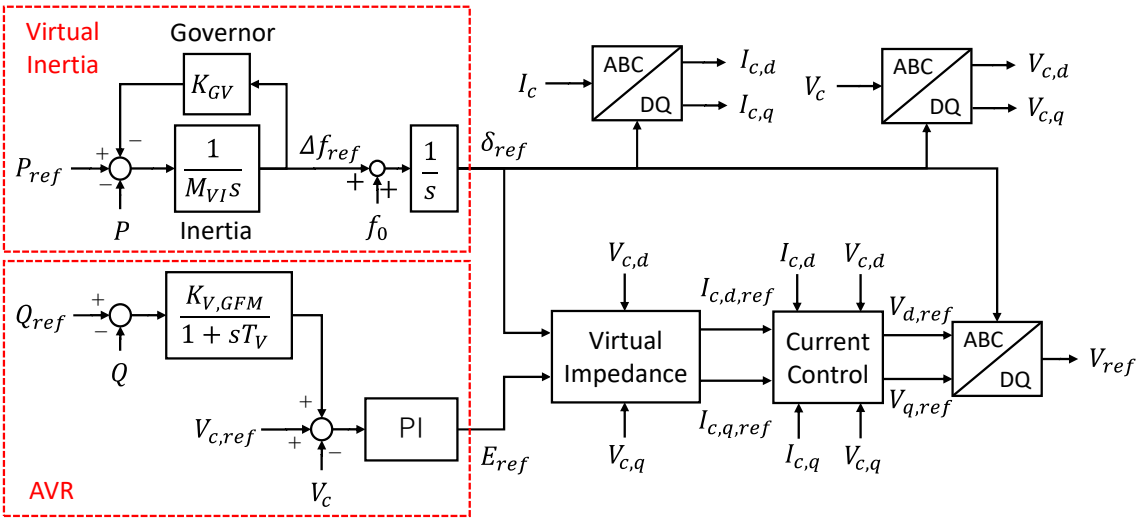

Figure 8. Controller model of the VI-GFM.

The current command $\boldsymbol{I_{c,ref}}\left(= I_{c,d,ref} + jI_{c,q,ref}\right)$ is implemented by the current controller. The virtual impedance and current control loop are not mandatory for VI-GFM, because $\boldsymbol{E_{ref}}$ can be used as a control order to the inverter. The advantage of the configuration is that current limitation can be easily implemented, as shown in Figure 5. The difference between the VI-GFL and VI-GFM is the dependency to the PLL. The VI-GFM does not need the PLL, except for synchronization at startup, because it uses the internal phase angle δ_{ref} as the reference for Park's transformation. Therefore, the VI-GFM is not affected by the instability of the PLL in a low-inertia system.

4. Condition of the Simulation Study

4.1. System Condition

The performance of the VI control was analyzed under certain conditions with varied IBR penetration rates (20%–80%). Table 1 lists the case indices of the simulation study. At Step 3, three control strategies were analyzed. The VI-GFL without voltage control and the VI-GFM were the existing strategies. The VI-GFL with voltage control was the proposed strategy.

Table 1. Indices of the simulation study.

Step	Source Connected as S3	S3 Capacity Ratio Corresponding to IBR Penetration Rate in Steps 2 and 3			
		20%	**40%**	**60%**	**80%**
1	Synchronous generator	#1-20	#1-40	#1-60	#1-80
2	IBR: conventional control	#2-20	#2-40	#2-60	#2-80
3	IBR: VI-GFL w/o voltage control	#3-GFL-20	#3-GFL-40	#3-GFL-60	#3-GFL-80
	IBR: VI-GFL with voltage control	#3-GFL-V-20	#3-GFL-V-40	#3-GFL-V-60	#3-GFL-V-80
	IBR: VI-GFM	#3-GFM-20	#3-GFM-40	#3-GFM-60	#3-GFM-80

Table 2 lists the power source capacity settings at each IBR penetration rate. The capacities of power sources S1 and S2 were changed depending on the IBR (S3) capacity to keep the system capacity the same among the cases. The rated capacity of the power source model was changed by the rated current while saving the rated voltage.

Table 2. Rated capacities of the generation units at each IBR penetration rate.

Percentage of S3 Capacity [1] (Means IBR PeneTration Rate in Step 2 and 3)	Rated Capacity [MVA]		
	S1 (SG [2])	**S2 (SG [2])**	**S3 (Step 1: SG [2], Step 2, 3: IBR)**
20%	120	120	60
40%	90	90	120
60%	60	60	180
80%	30	30	240

[1] SD is not considered in the percentage. The capacity of SD is 10 MVA in all cases. [2] SG denotes the synchronous generator.

The load condition was assumed to be 81.7% of the system capacity and was distributed equally to each load. Reactive power loads were set such that the power factor at each load bus did not change from the value in the original system model. Moreover, SD had 1.7% of the load, and the remaining 80% was shared among S1, S2, and S3 at the ratio of the rated capacities.

4.2. Parameter Setting

The parameter of the synchronous generator was set to the original value based on the IEEE 9-bus system. Figure 1 demonstrates the impedances of the transmission line and transformer. Table 3 lists the IBR control parameters. The virtual inertia constant M_{VI} and governor gain K_{GV} were set similarly as S3 in the Step 1 simulation. The voltage control parameter $K_{V,GFL}$ and $K_{V,GFM}$ were set so that the droop characteristics were not different between the VI-GFL and VI-GFM. The other parameters were determined by trial and error. The filter time constant T_f and T_V, and time window T_W were at risk of causing instability of the control if too-small values were set. The range of the values that enabled stable operations depended on the power grid configuration and the other control parameters.

Table 3. Control parameters of the IBR.

	Control Parameter	**Letter**	**Value**
GFL/GFM	Virtual inertia constant	M_{VI}	4.70 (s)
	Virtual governor gain	K_{GV}	25.0
GFL	Voltage control gain of VI-GFL	$K_{V,GFL}$	10.0
	Filter time constant in RoCoF computation	T_f	0.10 (s)
	Time window in RoCoF computation	T_W	0.10 (s)
GFM	Voltage control gain of VI-GFM	$K_{V,GFM}$	0.10
	Filter time constant of voltage control	T_V	0.02 (s)

5. Simulation Result

This section presents the results of the simulation study. Sections 5.1 and 5.2 present a detailed discussion of the results for the cases with 20% and 80% IBR penetration rates, respectively. Section 5.3 discusses the contribution of the VI control to the frequency stability, considering the transition from a synchronous generator-dominated system to an IBR-dominated system.

5.1. Twenty Percent IBR Penetration Rate

Figure 9 shows the simulation results for the cases with a 20% IBR penetration rate (#1-20, #2-20, #3-GFL-20, #3-GFL-V-20, and #3-GFM-20). Figure 9a shows the time variance of the center of inertia (COI) frequency f_{COI}, defined as Equation (6).

$$f_{COI}(t) = \frac{\sum_{i=1}^{N_G} M_i f_i(t)}{\sum_{i=1}^{N_G} M_i} \quad (6)$$

where M_i is the inertia constant of generator #i, f_i is the rotating frequency of generator #i, and N_G is the index number of generators. The COI frequency represents the average frequency of the generators, which is used to evaluate the frequency stability of the whole power system. The rotating frequency of each synchronous generator includes a component of eigenoscillation, and it should not be ignored when the local frequency stability or phase angle stability is discussed. For the stable operation of the power system, both the COI frequency change and the eigenoscillation should be suppressed. This paper mainly discusses the whole system frequency stability based on the COI frequency, but the influence of the VI control on the eigenoscillation is also discussed in this section.

For Step 2, the frequency at the POI of the IBR was not included in the COI frequency computations, because the IBR had neither inertia nor VI. However, for VI-GFL in Step 3, the frequency at the POI of the IBR with VI-GFL was excluded from the computation of the COI frequency, although VI-GFL had a VI, because VI-GFL controlled the phase angle of the IBR output voltage to follow that of the POI voltage. This indicated that the VI-GFL was not frequency-independent from the grid frequency. Meanwhile, the frequency at the POI of the IBR for VI-GFM in Step 3 was included in the COI frequency, computation because VI-GFM had a unique frequency that was internally independent of the grid frequency.

The frequency in case #2-20 significantly varied after the generator SD trip, compared with the other cases, because the conventional control did not cover the disturbance, as shown in Figure 9b, which describes the deviation of the active power output of S3 from the value just before the disturbance occurred. The VI control quickly responded in a few seconds and largely reduced the frequency deviation, regardless of its implementation method. The reduction of the maximum frequency deviation was considered to be a contribution of the responsivity of the governor function in the VI controls. The governor function in the VI control could respond without such delay, while the governor of the synchronous generator took approximately 10 s to cover the power variation for a time delay in the mechanical part response and the frequency deadband in the controller. Among the VI controls, the responses to the disturbance showed no significant differences, but VI-GFM responded more quickly than the other two, because VI-GFL required time to detect the frequency using the PLL. The influence of the voltage control function on the VI-GFL performance was not observed. Additionally, the inertia response of S3, a sudden power increase just after the disturbance occurrence, seemed to be small compared with the disturbance (5-MW generation loss). In this case, the capacity of S3 was small, and the load sharing was also small. Another reason was that the load demand decreased by a voltage dip, because the active power load was modeled as a constant current characteristic.

Figure 9c shows the deviation of the voltage at the POI of S3 from the value just before the disturbance occurrence. The voltage reduction in all cases was less than 0.35% of the nominal value (13.8 kV), and a large impact was not observed. This was because there were synchronous generators with at least 80% of the system capacity, which was

sufficient to maintain the voltage. Moreover, the voltage reduction was relatively large for cases #2-20 and #3-GFL-20, because the reactive power did not respond to the voltage change, as shown in Figure 9d. However, the VI-GFL with voltage control regulated the reactive power against the voltage variation and suppressed this variation. Immediately after the disturbance occurred, the voltage variation in #3-GFL-V-20 was larger than that in #3-GFM-20, but after that, both provided equivalent performances.

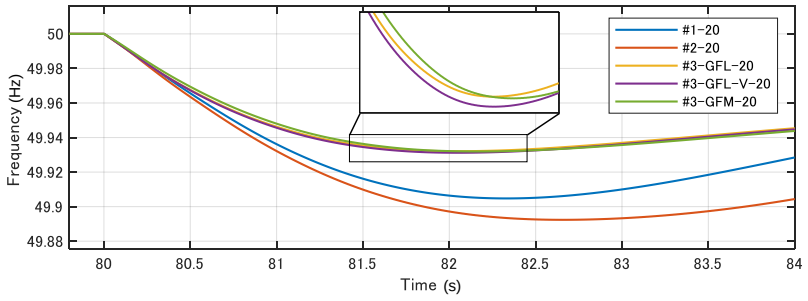

(**a**)

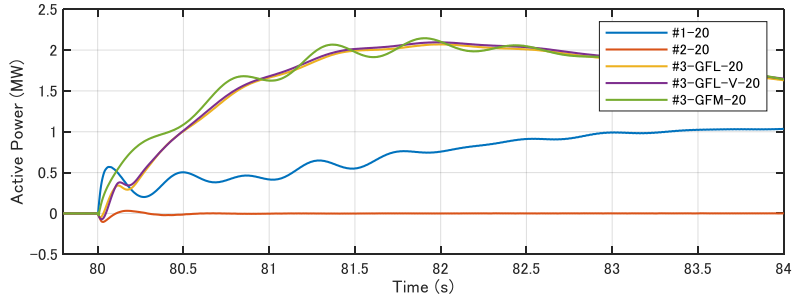

(**b**)

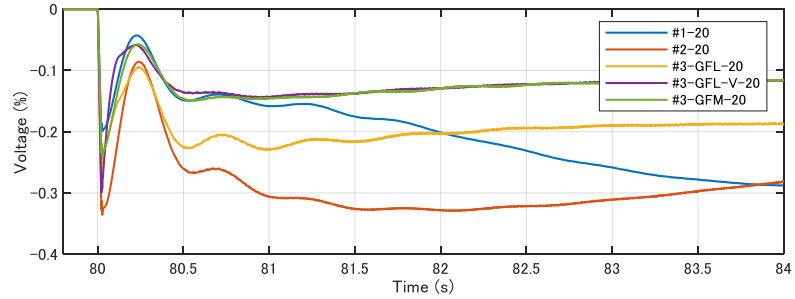

(**c**)

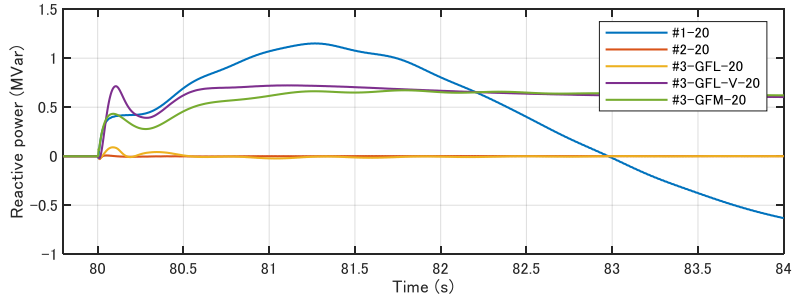

(**d**)

Figure 9. Simulation result of the cases for the 20% IBR penetration rate (disturbance was a 5-MW generation loss). (**a**) COI frequency, (**b**) the deviation of the active power output of S3, (**c**) the deviation of the voltage at the POI of the IBR, and (**d**) the deviation of the reactive power output of S3.

5.2. Eighty Percent IBR Penetration Rate

Figure 10 shows the results when the IBR penetration rate was 80%. Figure 10a shows the COI frequency. The frequency variation in #1-80 was larger than that in #1-20. This was because the system inertia, which was the total kinetic energy, was small in #1-80 for the small inertia constant of S3. In #2-80, the COI frequency rapidly dropped after the disturbance and did not recover to a stable state. In a system with low inertia, the frequency change was too fast for the governor to cover the disturbance, resulting in frequency divergence. In Step 3 (cases #3-GFL-80, 3-GFL-V-80, and #3-GFM-80), the frequency variation could be significantly reduced. In particular, VI-GFM reduced the change rate of the frequency.

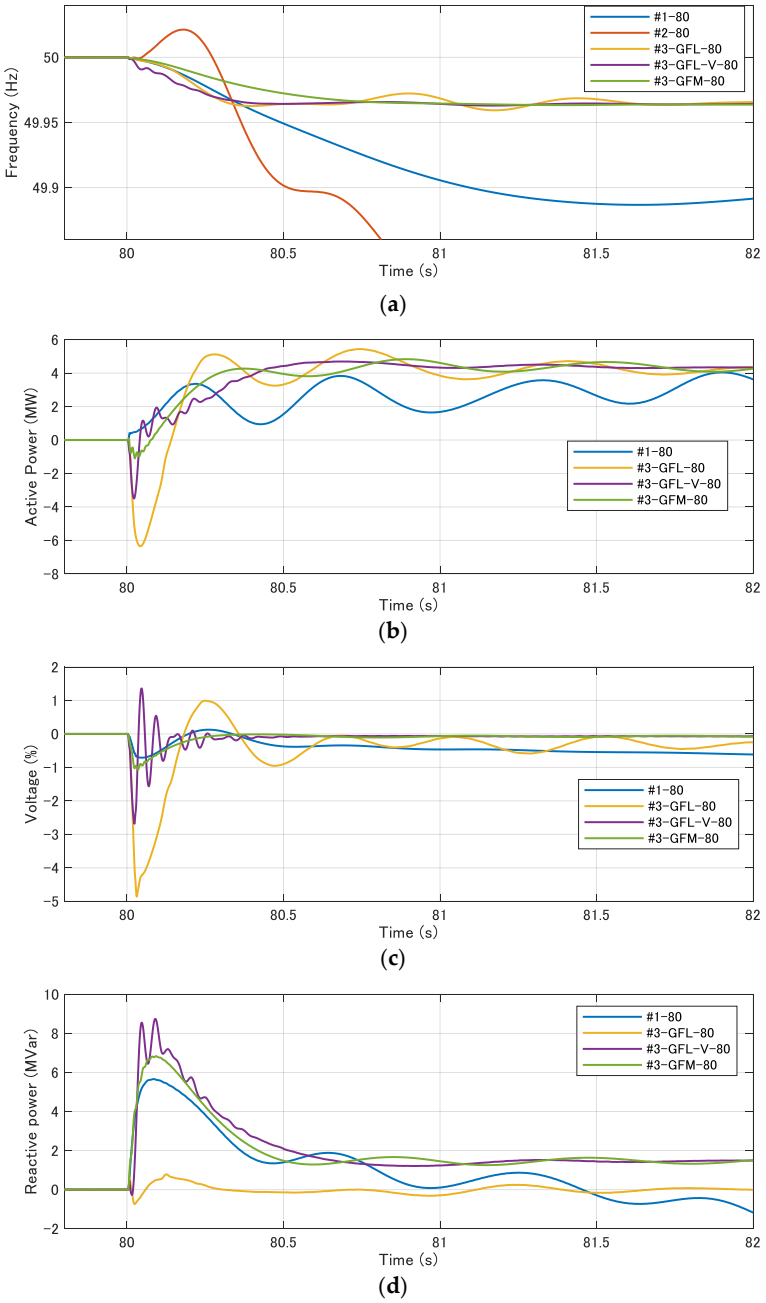

Figure 10. Simulation results of the cases for the 80% IBR penetration rate. (**a**) COI frequency, (**b**) the deviation of the active power output of S3, (**c**) the deviation of the voltage at the POI of the IBR, and (**d**) the deviation of the reactive power output of S3.

Figure 10b shows that the IBR with the VI control responded to the disturbance quickly and reached the desired sharing level within a second. However, the output power of the IBR temporarily decreased immediately after the disturbance, because the voltage at the POI of the IBR decreased, as shown in Figure 10c. Specifically, the voltage at the POI of S3 (synchronous generator) for case #1-80 decreased by a maximum of 0.7%. However, a larger drop was evident in the other cases, including 1.1% in #3-GFM-80, 2.7% in #3-GFL-V-80, and 4.9% in #3-GFL-80 and #2-80. The results showed that the voltage control function for the VI-GFL could effectively improve the transient voltage behavior and active power response of the VI function. Figure 10d shows that the reactive power response provided by the voltage control function is as fast as that of VI-GFM and the synchronous generator.

Moreover, the contribution of the voltage control function for the VI-GFL was apparent in the eigenoscillation among the synchronous generators. Figure 11 shows the frequency of the synchronous generators. Moreover, the oscillation between S1 and S2 for case #3-GFL-80 was larger than that in #1-80, but the activation of the voltage control function reduced the oscillation to the same level as in #3-GFM-80, as shown in Figure 11c,d. Thus, the synchronizing force acting between the generators was maintained by suppressing the voltage drop, because it depended on the voltage. Therefore, the voltage control function for VI-GFL was important for maintaining the frequency stability.

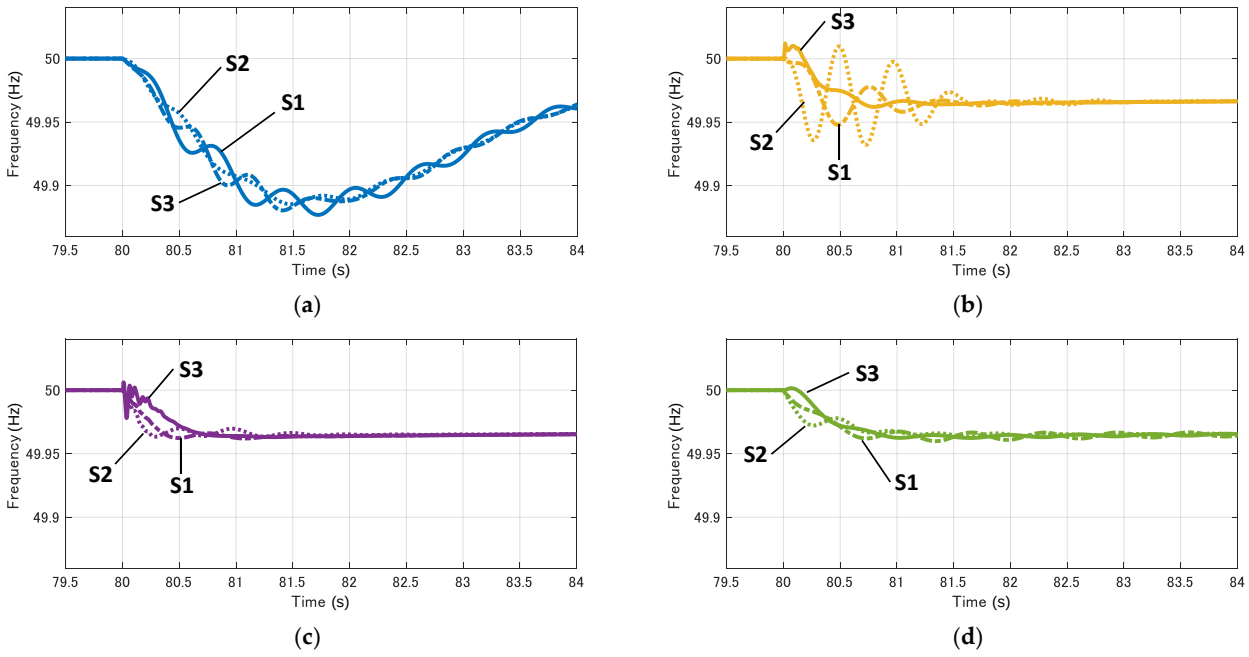

Figure 11. Frequency of the synchronous generators (IBR penetration rate was 80%) (**a**) #1-80, (**b**) #3-GFL-80, (**c**) #3-GFL-V-80, and (**d**) #3-GFM-80.

5.3. Comparison among All Penetration Levels

This section presents the results of all the cases briefly using an evaluation index of the frequency stability and discusses its transition by increasing the IBR penetration level. The frequency stability is evaluated by the index "*Nadir*," which is the frequency nadir of the COI frequency, as in Equation (7), and "*RoCoF*," which is the maximum change rate of the COI frequency that emerges until the COI frequency reaches *Nadir*, as in Equations (8) and (9).

$$Nadir = \min_{t} f_{COI}(t) \tag{7}$$

$$RoCoF = \max_{i=1,2,\cdots,K} \frac{|f_{COI}(t_0 + i\,T_s) - f_{COI}(t_0 + (i-1)T_s)|}{T_s} \tag{8}$$

$$K = \max\left\{ n \in \mathbb{Z} \;\middle|\; n \leq \frac{t_{nadir} - t_0}{T_s} \right\} \tag{9}$$

where t_0 is the time of disturbance occurrence, t_{nadir} is the time when the frequency reaches *Nadir*, and T_s is the length of the time window. The COI frequency is used for computing the evaluation index to evaluate the average behavior of the system. Moreover, the time window for the computation of *RoCoF* is a necessary concept according to several studies [38,39]. As shown in Figure 10a, the frequency reaches *Nadir* within 500 ms under a large IBR penetration. Therefore, the time window T_s was set to 100 ms in this evaluation.

Figure 12 shows the relationship between *Nadir* and *RoCoF* for all cases. In Step 1, *Nadir* decreased and *RoCoF* increased as the capacity of S3 increased, owing to the small inertia constant of S3 compared to those of S1 and S2, which were previously mentioned in Section 5.2. In Step 2, *Nadir* decreased and *RoCoF* increased, because the IBR did not recover the frequency stability. The results for #2-60 and #2-80 are not shown in Figure 12, because the frequency is not stabilized in those cases. Finally, in Step 3, *Nadir* increased as the IBR penetration rate increased, despite the implementation of the VI function. The VI-GFM also improved *RoCoF* drastically from Step 1. This came from the fast responsivity of the governor function of VI-GFM. As shown in Figures 9 and 10, the response of the governor control of the VI-GFM was much faster than the synchronous generator, because the governor of the VI-GFM had no delay and a deadband in the controller, as explained in Section 3, and it was considered that the fast responsivity helped suppress the deacceleration of the synchronous generators. The contribution of the voltage control function was only at most 6.2% at the 80% IBR penetration rate. However, compared with the results in Step 1, *RoCoF* was not worse. This indicated that the VI-GFL can maintain *RoCoF* at the same level as the synchronous generator-dominated system.

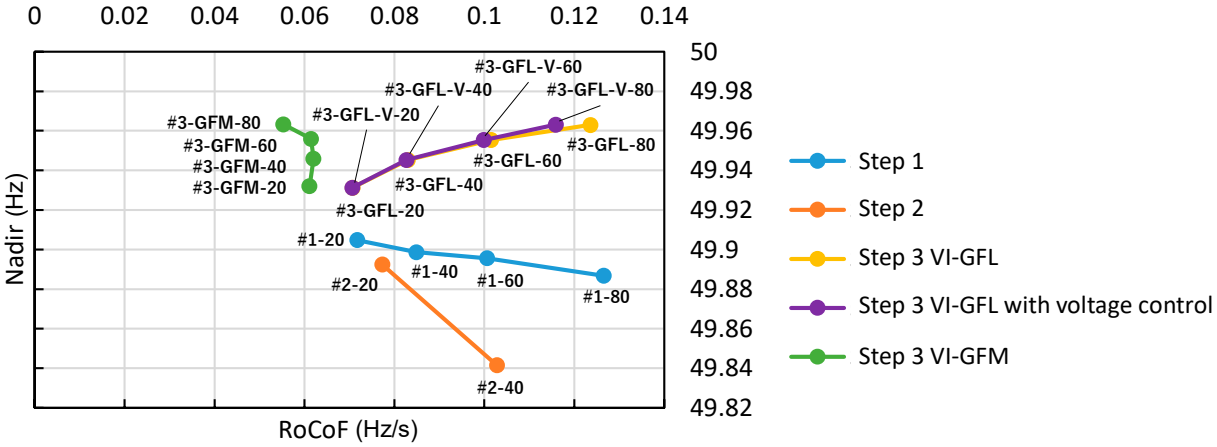

Figure 12. Indexed frequency stability for all cases.

6. Discussion and Conclusions

There are several types of methodologies in implementing the VI function in IBRs. The performance of these IBRs with VI controls must be clarified to develop a stable future power grid that is highly penetrated by IBRs. This study analyzed the frequency regulation capability of the VI control implemented on both the GFL-type and GFM-type. In particular, as a novelty of this paper, the analysis focused on the contribution of the voltage control function available for the GFL-type control to the performance of the VI control. The simulation study clarified that the voltage control function can reduce the voltage fluctuation after faults, resulting in an improved active power response of the VI-GFL. Moreover, the eigenoscillation among the synchronous generators can be suppressed by the voltage control function. As for the stability of the system frequency, the VI-GFL performed well in improving the *Nadir* at the same level as the VI-GFM but could not improve the *RoCoF* as much as the VI-GFM. However, the *RoCoF* was slightly better than

that in the synchronous generator-dominated system, which indicates the possibility that VI-GFL can maintain a frequency stability without VI-GFM.

The improvement of the VI-GFL performance on stabilizing the power system and improving the frequency stability discussed in this study is crucial in real-world applications, because the conventional IBR has a GFL-type controller, and there is a lower barrier for the adoption of VI-GFL, compared with VI-GFM. Therefore, VI-GFL is expected to be applied to IBRs in the short- to mid-term future owing to high expectations for the early realization of the large penetration of renewable energy resources.

However, there are still problems to be solved in order to broaden the adoption of VI-GFL. In this study, the IBR was modeled as an integrated one composed of so many units, and high-voltage interconnection was assumed. Meanwhile, in real-world applications, a large number of small-scale IBRs are connected in various voltage classes. In those situations, the performances of individual IBR are expected to be different, and interferences also occur. To analyze the performance of the IBRs with VI functioning at a high accuracy, the influence of that should be considered. This will be one of the important future works. In addition, the effectiveness of the VI controls for more critical disturbances like short-circuit faults needs to be evaluated to clarify the differences between VI-GFL and VI-GFM.

Author Contributions: Conceptualization, D.O. and H.T.; validation, D.O., H.K., T.T., T.O. and H.T.; investigation, D.O. and H.T.; writing—original draft preparation, D.O. and H.T.; supervision, K.O., T.O. and J.H.; and project administration, T.M., S.M., H.H. and K.M. All authors have read and agreed to the published version of the manuscript.

Funding: This study was based on the results obtained from a project commissioned by the New Energy and Industrial Technology Development Organization (NEDO), No. JPNP19002.

Acknowledgments: We would like to thank Yohei Kumagai for technical support of the simulations done in this study.

Conflicts of Interest: The authors declare no conflict of interest.

References

1. Hawaiian Electric Power Company. Rule No.14 Service Connections and Facilities on Customer's Premises. Available online: https://www.hawaiianelectric.com/documents/billing_and_payment/rates/hawaiian_electric_rules/14.pdf (accessed on 14 May 2021).
2. Pacific Gas and Electric Company (PG&E). Electric Rule No.21 Generating Facility Interconnections. Available online: https://www.pge.com/tariffs/assets/pdf/tariffbook/ELEC_RULES_21.pdf (accessed on 14 May 2021).
3. Yap, K.Y.; Charles, C.R.; Lim, J.M.-Y. Virtual Inertia-Based Inverters for Mitigating Frequency Instability in Grid-Connected Renewable Energy System: A Review. *Appl. Sci.* **2019**, *9*, 5300. [CrossRef]
4. Unruh, P.; Nuschke, M.; Strauß, P.; Welck, F. Overview on Grid-Forming Inverter Control Methods. *Energies* **2020**, *13*, 2589. [CrossRef]
5. Tamrakar, U.; Shrestha, D.; Maharjan, M.; Bhattarai, B.P.; Hansen, T.M.; Tonkoski, R. Virtual Inertia: Current Trends and Future Directions. *Appl. Sci.* **2017**, *7*, 654. [CrossRef]
6. *Basic Classification of Inverters*; Technical Update; Electric Power Research Institute: Palo Alto, CA, USA, 26 November 2019.
7. Lin, Y.; Eto, J.H.; Johnson, B.B.; Flicker, J.D.; Lasseter, R.H.; Pico, H.N.V.; Seo, G.; Pierre, B.J.; Ellis, A. *Research Roadmap on Grid-Forming Inverters*; NREL Technical Report for National Renewable Energy Lab: Golden, CO, USA, 2020.
8. Matevosyan, J.; Badrzadeh, B.; Prevost, T.; Quitmann, E.; Ramasubramanian, D.; Urdal, H.; Huang, S.H.; Vital, V.; O'Sullivan, J.; Quint, R. Grid-Forming Inverters: Are They the Key for High Renewable Penetration? *IEEE Power Energy Mag.* **2019**, *17*, 89–98. [CrossRef]
9. Tayyebi, A.; Groß, D.; Anta, A.; Kupzog, F.; Dörfler, F. Frequency Stability of Synchronous Machines and Grid-Forming Power Converters. *IEEE J. Emerging Sel. Top. Power Electron.* **2020**, *8*, 1004–1018. [CrossRef]
10. Paolone, M.; Gaunt, T.; Guillaud, X.; Liserre, M.; Meliopoulos, S.; Monti, A.; van Cutsem, T.; Vittal, V.; Vournas, C. Fundamentals of power systems modelling in the presence of converter-interfaced generation. *Electr. Power Systems Res.* **2020**, *189*, 106811. [CrossRef]
11. Key, T.; Kou, G.; Jensen, M. On Good Behavior: Inverter-Grid Protections for Integrating Distributed Photovoltaics. *IEEE Power Energy Mag.* **2020**, *18*, 75–85. [CrossRef]

12. Gui, Y.; Wang, X.; Blaabjerg, F.; Pan, D. Control of Grid-Connected Voltage-Source Converters: The Relationship Between Direct-Power Control and Vector-Current Control. *IEEE Ind. Electron. Mag.* **2019**, *13*, 31–40. [CrossRef]
13. Kroposki, B.; Johnson, B.; Zhang, Y.; Gevorgian, V.; Denholm, P.; Hodge, B.; Hannegan, B. Achieving a 100% Renewable Grid: Operating Electric Power Systems with Extremely High Levels of Variable Renewable Energy. *IEEE Power Energy Mag.* **2017**, *15*, 61–73. [CrossRef]
14. Odogwu, I.G. Phase-Locked Loop Control in Low-Inertia Grid- Connected Voltage-Source Converters. Bachelor's Thesis, Georgia Southern University, Statesboro, GA, USA, 2020.
15. Juan, G.; Rueda-Escobedo, J.G.; Tang, S.; Schiffer, J. A Performance Comparison of PLL Implementations in Low-Inertia Power Systems Using an Observer-Based Framework. *IFAC-PapersOnLine* **2020**, *53*, 12244–12250.
16. Sun, Y.; de Jong, E.C.W.; Wang, X.; Yang, D.; Blaabjerg, F.; Cuk, V.; Cobben, J.F.G. The impact of PLL dynamics on the low inertia power grid: A case study of Bonaire island power system. *Energies* **2019**, *12*, 1–16. [CrossRef]
17. Aemo. Black System South Australia 28 September 2016–Final Report. Available online: https://aemo.com.au/-/media/files/electricity/nem/market_notices_and_events/power_system_incident_reports/2017/integrated-final-report-sa-black-system-28-september-2016.pdf?la=en&hash=7C24C97478319A0F21F7B17F470DCA65 (accessed on 14 May 2021).
18. National Grid ESO. Technical Report on the events of 9 August 2019. Available online: https://www.nationalgrideso.com/document/152346/download (accessed on 14 May 2021).
19. Elkhatib, M.E.; Du, W.; Lasseter, R.H. Evaluation of Inverter-based Grid Frequency Support using Frequency-Watt and Grid-Forming PV Inverters. In Proceedings of the 2018 IEEE Power & Energy Society General Meeting (PESGM), Portland, OR, USA, 5–10 August 2018; pp. 1–5.
20. Pattabiraman, D.; Lasseter, R.H.; Jahns, T.M. Comparison of Grid Following and Grid Forming Control for a High Inverter Penetration Power System. In Proceedings of the 2018 IEEE Power & Energy Society General Meeting (PESGM), Portland, OR, USA, 5–10 August 2018; pp. 1–5.
21. Datta, U.; Kalam, A.; Shi, J. Frequency performance analysis of multi-gain droop controlled DFIG in an isolated microgrid using real-time digital simulator. *Eng. Sci. Technol. Int. J.* **2020**, *23*, 1028–1041. [CrossRef]
22. Liu, J.; Miura, Y.; Ise, T. Comparison of Dynamic Characteristics between Virtual Synchronous Generator and Droop Control in Inverter-Based Distributed Generators. *IEEE Trans. Power Electron.* **2016**, *31*, 3600–3611. [CrossRef]
23. Yazdi, S.S.H.; Milimonfared, J.; Fathi, S.H.; Rouzbehi, K.; Rakhshani, E. Analytical modeling and inertia estimation of VSG-controlled Type 4 WTGs: Power system frequency response investigation. *Int. J. Electr. Power Energy Syst.* **2019**, *107*, 446–461. [CrossRef]
24. Xi, j.; Geng, H. Decoupling Control Scheme for VSG-WPPs to Participate in Grid Frequency Response. *IEEE Trans. Ind. Appl.* **2019**, *55*, 6368–6375. [CrossRef]
25. Fini, M.H.; Golshan, M.E.H. Determining optimal virtual inertia and frequency control parameters to preserve the frequency stability in islanded microgrids with high penetration of renewables. *Electr. Power Syst. Res.* **2018**, *154*, 13–22. [CrossRef]
26. Beltran, O.; Peña, R.; Segundo, J.; Esparza, A.; Muljadi, E.; Wenzhong, D. Inertia estimation of wind power plants based on the swing equation and Phasor Measurement Units. *Appl. Sci.* **2018**, *8*, 2413. [CrossRef]
27. Qoria, T.; Gruson, F.; Colas, F.; Kestelyn, X.; Guillaud, X. Current limiting algorithms and transient stability analysis of grid-forming VSCs. *Electr. Power Syst. Res.* **2020**, *189*, 106726. [CrossRef]
28. Qoria, T.; Gruson, F.; Colas, F.; Denis, G.; Prevost, T.; Guillaud, X. Critical Clearing Time Determination and Enhancement of Grid-Forming Converters Embedding Virtual Impedance as Current Limitation Algorithm. *IEEE J. Emerg. Sel. Top. Power Electron.* **2020**, *8*, 1050–1061. [CrossRef]
29. Zhang, X.; Zhu, Z.; Fu, Y.; Shen, W. Multi-objective virtual inertia control of renewable power generator for transient stability improvement in interconnected power system. *Int. J. Electr. Power Energy Syst.* **2020**, *117*, 105641. [CrossRef]
30. Zhang, X.; Zhu, Z.; Fu, Y.; Li, L. Optimized virtual inertia of wind turbine for rotor angle stability in interconnected power systems. *Electr. Power Syst. Res.* **2020**, *180*, 106157. [CrossRef]
31. Roos, P. A Comparison of Grid-Forming and Grid-Following Control of VSCs. Independent thesis Advanced level (professional degree), Uppsala University, Uppsala, Sweden, 2020.
32. Hirase, Y.; Uezaki, K.; Orihara, D.; Kikusato, H.; Hashimoto, J. Characteristic Analysis and Indexing of Multimachine Transient Stabilization Using Virtual Synchronous Generator Control. *Energies* **2021**, *14*, 2021. [CrossRef]
33. Anderson, P.M.; Fouad, A.A. *Power System Control. and Stability*, 2nd ed.; IEEE Press: Piscataway, NJ, USA, 2003; pp. 13–52, 83–148.
34. Institution of Electrical Engineering in Japan. Japanese Power System Model. Available online: http://www.iee.or.jp/pes/model/english/ (accessed on 17 May 2021).
35. Simões, M.G.; Palle, B.; Chakraborty, S.; Uriarte, C. *Electrical Model Development and Validation for Distributed Resources*; Subcontract Report NREL/SR-581-41109; National Renewable Energy Laboratory: Golden, CO, USA, 2007.
36. Kaura, V.; Blasko, V. Operation of a Phase Locked Loop System under Distorted Utility Conditions. *IEEE Trans. Ind. Appl.* **1997**, *33*, 58–63. [CrossRef]
37. Rowan, T.M.; Kerkman, R.J. A New Synchronous Current Regulator and an Analysis of Current-Regulated PWM Inverters. *IEEE Trans. Ind. Appl.* **1986**, *IA-22*, 678–690. [CrossRef]

38. RG-CE System Protection & Dynamics Sub Group. *Frequency Measurement Requirements and Usage Final Version 7*; ENTSO-e: Brussels, Belgium, 2018.
39. Crivellaro, A.; Tayyebi, A.; Gavriluta, C.; Groβ, D.; Anta, A.; Kupzog, F.; Dörfler, F. Beyond low-inertia systems: Massive integration of grid-forming power converters in transmission grids. In Proceedings of the IEEE Power & Energy Society General Meeting (PESGM), Montreal, QC, Canada, 2–6 August 2020; p. 1086.